Sol−Gel Pure and Mixed-Phase Titanium Dioxide for Photocatalytic Purposes: Relations between Phase Composition, Catalytic Activity, and Charge-Trapped Sites

Roberto Scotti,*[,†] Ignazio Renato Bellobono,[‡] Carmen Canevali,[†] Carla Cannas,[§] Michele Catti,[†] Massimiliano D'Arienzo,[†] Anna Musinu,[§] Stefano Polizzi,[||] Marco Sommariva,[†] Andrea Testino,[†] and Franca Morazzoni[†]

INSTM, Department of Materials Science, University of Milano-Bicocca, Via R. Cozzi 53, I-20125 Milano, Italy, Department of Physical Chemistry, Environmental Research Centre, University of Milano, Via Golgi 19, I-20133 Milano, Italy, Department of Scienze Chimiche, University of Cagliari, SS554 Bivio per Sestu, 09042 Monserrato (CA), Italy, and Department of Physical Chemistry, University of Venezia, Via Torino 155/b, I-30172 Venezia, Italy

Received February 15, 2008. Revised Manuscript Received April 1, 2008

The sol−gel synthesis of TiO_2 from $TiCl_4$ assisted by the triblock copolymer $EO_{20}-PO_{70}-EO_{20}$ (EO = $-CH_2CH_2O-$, PO = $-CH_2(CH_3)CHO-$) as templating agent was carried out by systematically changing H_2O:Ti (r_w) and HCl:Ti (r_a) molar ratios. Mesoporous and nanocrystalline TiO_2 samples with well-defined and controlled phase composition (anatase, rutile, and mixed phase) were obtained after calcination at 400 °C and characterized for the morphology, particle size, and shape using TEM, HRTEM, XRD, and surface area measurements. The role of r_w and r_a and influence of the copolymer in determining the phase composition was demonstrated. Rutile becomes the main phase by increasing r_w. In fact, the decrease of Ti concentration slows down the condensation rate, favoring formation of rutile seeds in the gel. The photocatalytic activity of TiO_2 in the UV photomineralization of phenol depends on the phase composition and oxidizing agent, H_2O_2 or O_2. When the oxidation is performed by H_2O_2, rutile, formed by large crystalline rods with high aspect ratios (size 15−20 × 100−120 nm), shows higher catalytic activity with respect to the small, almost cubic, anatase particles (5−15 nm). If O_2 is used, the catalytic activity generally decreases and the behavior of polymorphous species is reverse. EPR investigation of the paramagnetic charge carriers, formed under UV irradiation at 10 K, showed the resonance lines of holes trapped at O^- lattice sites and electrons trapped at Ti^{3+} and O_2^- sites. The rutile crystalline rods present the largest quantity of O^- and Ti^{3+} centers. The overall results suggest correlation between TiO_2 particle size and shape and the photocatalytic activity and indicate that electron−hole recombination is the most probable rate-controlling process.

1. Introduction

For about 10 years there have been many reports in the literature about TiO_2 synthesized via different routes due to its promise in photocatalytic oxidative processes such as the photodegradation of organic pollutants in air or water at room temperature and pressure.[1] In spite of the huge number of scientific contributions in which TiO_2 powders with different crystalline phase, morphology, particle shape, and size were examined, the relationships between morphological and structural properties and the catalytic behavior still remain unclear. Contrasting opinions were reported about the influence of the crystalline phase on the photocatalytic properties. Different authors state that anatase works better than rutile,[2] while others showed the best activity for rutile[3] or the existence of synergistic effects in the photocatalytic activity[4] for anatase−rutile mixed phases.

In addition, several efforts were carried out to obtain highly porous TiO_2, powder or film,[5] with the aim of improving the catalytic activity. Nevertheless, although the effects of porosity combined with those of the particle nanodimension were demonstrated in anatase,[5j] the catalytic performance of these materials was not systematically discussed in connection with the particle shape and dimension and structural properties.

Photoexcitation of TiO_2 generates electron−hole (e^-−h^+) pairs which play a key role in photocatalytic processes. In fact, e^-−h^+ pairs, if they do not recombine, can be trapped

* To whom correspondence should be addressed. E-mail: Roberto.Scotti@unimib.it.
† University of Milano-Bicocca.
‡ University of Milano.
§ University of Cagliari.
|| University of Venezia.

(1) (a) Hoffmann, M. R. *J. Phys. Chem. B* **2005**, *109*, 8673. (b) Hoffman, M. R.; Martin, S. T.; Choi, W. *Chem. Rev.* **1995**, *95*, 69–96. (c) Carp, O.; Huisman, C. L.; Reller, A. *Prog. Solid State Chem.* **2004**, *32*, 33–177. (d) Thompson, T. T.; Yates, J. T. *Chem. Rev.* **2006**, *106*, 4428–4453.
(2) Linsebigler, A. L.; Lu, G.; Yates, J. T. *Chem. Rev.* **1995**, *95*, 735.
(3) (a) Watson, S. S.; Beydoun, D.; Scott, J. A.; Amal, R. *Chem. Eng.J.* **2003**, *95*, 213. (b) Mills, A.; Lee, S. K.; Lepre, A. *J. Photochem. Photobiol. A* **2003**, *155*, 199. (c) Habibi, M. H.; Vosooghian, H. *J. Photochem. Photobiol. A* **2005**, *174*, 45.
(4) (a) Bacsa, R. R.; Kiwi, J. *Appl. Catal., B* **1998**, *16*, 19. (b) Watson, S.; Beydoun, D.; Scott, J.; Amal, R. *J. Nanoparticle Res.* **2004**, *6*, 193. (c) Yan, M.; Chen, F.; Zhang, J.; Anpo, M. *J. Phys. Chem. B* **2005**, *109*, 8673.

10.1021/cm800465n CCC: $40.75
Published on Web 06/04/2008

as Ti^{3+} and O^- defect sites of the TiO_2 lattice or react with oxidative species (e.g., H_2O_2 or O_2) and chemisorbed OH^- groups. Such reactions generate $OH^\bullet$ radicals, which oxidize the organic substrates until CO_2.[6] Several studies have been published aimed to identify the postirradiation paramagnetic defects[7–9] by means of electron paramagnetic resonance (EPR) spectroscopy. They were performed mainly on anatase[8,9a,c–e] or the commercial P25 mixed phase.[7,9e] Significantly Kumar investigated trapped electrons and holes in pure rutile and anatase,[9b] and Murphy studied the O_2^- chemisorption on a TiO_2 surface;[9f,g] however, none of these authors tried to relate the amount of charge-trapping species with the TiO_2 photocatalytic activity in a set of samples as a function of phase composition, morphology, particle size, and oxidative agent.

It is our opinion that useful relations between morphology, particle size and shape, crystalline phase, and defect centers, on one hand, and photocatalytic activity, on the other hand, may be obtained by investigating a large number of samples with controlled phase composition, prepared using the same synthesis method. We recently carried out an extensive study on hydrothermally synthesized TiO_2 powders with known crystalline phase, particle morphology, porosity, and surface area.[10] It was shown that a strong correlation exists between the photocatalytic activity in the photodegradation of aqueous phenol in the presence of H_2O_2 and the particle size and shape of the catalysts: prismatic rutile particles with an aspect ratio α (length:width) ≈ 5 and length of 60−100 nm showed the highest activity. These results suggested that the electron−hole recombinations in particles with different crystallinity are rate-controlling steps in the photocatalytic process.

In an attempt to design the photocatalytic activity of TiO_2 nanoparticles by tailoring their crystalline phase and size shape, the sol−gel method is another common route used to prepare TiO_2 samples with reproducible properties. Many authors used titanium alkoxides as precursors.[11–14] The morphological and structural properties of the resulting samples depend on the water:alkoxide ratio, acid/base catalyst, solvent type, gel aging, reaction temperature, and mixing technique. Generally, pure anatase or mixed phase has been obtained from alkoxide precursors. Pure rutile was produced by heating the powders at temperatures higher than 400 °C, which also causes undesired grain coarsening, aggregation, and reduction of the surface area[14] or, alternatively, crystallization under hydrothermal conditions.[15]

Thermohydrolysis of $TiCl_4$[16] in aqueous medium was proposed as an alternative soft-chemistry method to prepare pure anatase as it allows one to control the particle size at the nanometric scale as a function of pH, but also in this case pure rutile was produced by treating the powders at high temperature. Different compositions of rutile, anatase, and brookite were obtained by thermohydrolysis and oxidation of $TiCl_3$,[17] accurately varying the pH between 0 and 7, but in this case brookite-free anatase could not be obtained.

Sanchez and co-workers[5i,k] reported on the hydrolysis and condensation of $TiCl_4$ in alcoholic solution in the presence of surfactant block copolymer as templating agent. Mesoporous anatase thin films were obtained, and the role of experimental variables, in particular of the water amount, was deeply investigated. Recently Yan et al.[18] prepared pure anatase, rutile, and mixed-phase mesoporous TiO_2 by a similar template approach that simply varies the phase composition by varying the alcohol used as solvent and the amount of water and HCl. This method makes the systematic investigation of the photocatalytic activity of TiO_2 materials feasible. The acidity drives phase formation; nevertheless, the synthesis conditions and role of water and acid need deeper study. In particular, when no water was added as reactant, the influence of the air moisture and solvent humidity is hardly reproducible; moreover, it was not considered that addition of aqueous HCl also changes the H_2O:Ti ratio besides the acidity.

(5) (a) Fujii, H.; Ohtaky, M.; Eguchi, K. *J. Am. Chem. Soc.* **1998**, *120*, 6832. (b) Yoshitake, H.; Sugihara, T.; Tatsumi, T. *Chem. Mater.* **2002**, *14*, 1023. (c) Antonelli, D. M. *Microporous Mesoporous Mater.* **1999**, *30*, 315. (d) Soler-Illia, G. J. A. A.; Louis, A.; Sanchez, C. *Chem. Mater.* **2002**, *14*, 750. (e) Yang, P.; Zhao, D.; Margolese, D.; Chmelka, B. F.; Stucky, G. D. *Nature* **1998**, *396*, 152. (f) Yue, Y.; Gao, Z. *Chem.Commun.* **2000**, 1755. (g) Tian, B.; Yang, H.; Liu, X.; Xie, S.; Yu, C.; Fan, J.; Tu, B.; Zhao, D. *Chem. Commun.* **2002**, 1824. (h) Kluson, P.; Kacer, P.; Cajthaml, T.; Kalaji, M. *J. Mater. Chem.* **2001**, *11*, 644. (i) Grosso, D.; Soler-Illia, G. J. A. A.; Crepaldi, E. L.; Cagnol, F.; Sinturel, C.; Bourgeois, A.; Brunet-Bruneau, A.; Amenitsch, H.; Albouy, P. A.; Sanchez, C. *Chem. Mater.* **2003**, *15*, 4562–4570. (j) Crepaldi, E. L.; Soler-Illia, G. J. A. A.; Grosso, D.; Cagnol, F.; Ribot, F.; Sanchez, C. *J. Am. Chem. Soc.* **2003**, *125*, 9770–9786. (k) Sakatani, Y.; Grosso, D.; Nicole, L.; Soler-Illia, G. J. A. A.; Sanchez, C. *J. Mater. Chem.* **2006**, *16*, 77–82.

(6) Sclafani, A.; Herrmann, J. M. *J. Phys. Chem.* **1996**, *100*, 13655.

(7) (a) Hurum, D. C.; Agrios, A. G.; Gray, K. A.; Rajh, T.; Thurnauer, M. C. *J. Phys. Chem. B* **2003**, *107*, 4545–4549. (b) Hurum, D. C.; Gray, K. A.; Rajh, T.; Thurnauer, M. C. *J. Phys. Chem. B* **2005**, *109*, 977–980. (c) Hurum, D. C.; Agrios, A. G.; Crist, S. E.; Gray, K. A.; Rajh, T.; Thurnauer, M. C. *J. Electron Spectrosc.* **2006**, *107*, 155–163. (d) Hurum, D. C.; Agrios, A. G.; Gray, K. A.; Rajh, T.; Thurnauer, M. C. *J. Phys. Chem. B* **2003**, *107*, 4545–4549.

(8) (a) Berger, T.; Sterrer, M.; Diwald, O.; Knözinger, E. *ChemPhysChem* **2005**, *6*, 2104–2112. (b) Berger, T.; Sterrer, M.; Stankic, S.; Bernardi, J.; Diwald, O.; Knözinger, E. *Mater. Sci. Eng. C* **2005**, *25*, 664–668. (c) Berger, T.; Sterrer, M.; Diwald, O.; Knözinger, E.; Panayotov, D.; Thompson, T. L.; Yates, J. T. *J. Phys. Chem. B* **2005**, *109*, 6061–6068. (d) Elser, J. E.; Berger, T.; Sterrer, M.; Brandhuber, D.; Bernardi, J.; Diwald, O.; Knözinger, E. *J. Phys. Chem. B* **2006**, *110*, 7605–7608. (e) Berger, T.; Diwald, O.; Knözinger, E.; Sterrer, M.; Yates, J. T. *Phys. Chem. Chem. Phys.* **2006**, *8*, 1822–1826.

(9) (a) Ke, S. C.; Wang, T. C.; Wong, M. S.; Gopal, N. O. *J. Phys. Chem. B* **2006**, *110*, 11628–11634. (b) Kumar, C. P.; Gopal, N. O.; Wang, T. C.; Wong, M. S.; Ke, S. C. *J. Phys. Chem. B* **2006**, *110*, 5223–5229. (c) Coronado, J. M.; Maira, A. J.; Conesa, C. J.; Yeung, K. L.; Augugliaro, V.; Soria, J. *Langmuir* **2001**, *17*, 5368–5374. (d) Yeung, K. L.; Yau, S. T.; Maira, A. J.; Coronado, J. M.; Soria, J.; Yue, P. L. *J. Catal.* **2003**, *17*, 107–116. (e) Coronado, J. M.; Soria, J. *Catal. Today* **2007**, *123*, 37–41. (f) Attwood, A. L.; Murphy, D. M.; Edwards, J. L.; Egerton, T. A.; Harrison, R. W. *Res. Chem. Intermed.* **2003**, *29*, 449–465. (g) Carter, E.; Carley, A. F.; Murphy, D. M. *J. Phys. Chem. C* **2007**, *111*, 10630–10638.

(10) Testino, A.; Bellobono, I. R.; Buscaglia, V.; Canevali, C.; D'Arienzo, M.; Polizzi, S.; Scotti, R.; Morazzoni, F. *J. Am. Chem. Soc.* **2007**, *129*, 3564–3575.

(11) Li, Y.; White, T. J.; Lim, S. H. *Solid State Chem.* **2004**, *177*, 1372–1381.

(12) Watson, S.; Beydoun, D.; Scott, J.; Amal, R. *J. Nanoparticles Res.* **2004**, *6*, 193–207.

(13) (a) Song, K. C.; Pratsinis, S. E. *J. Colloid Interface Sci.* **2000**, *231*, 289–298. (b) Song, K. C.; Pratsinis, S. E. *J. Am. Ceram. Soc.* **2001**, *84*, 92–98.

(14) Li, G.; Gray, K. A. *Chem. Mater.* **2007**, *19*, 11431146) .

(15) Bacsa, R. R.; Kiwi, J. *Appl. Catal. B: Environ.* **1998**, *16*, 19–29.

(16) Pottier, A.; Cassaignon, S.; Chaneac, C.; Villain, F.; Tronc, E.; Jolivet, J.-P. *J. Mater. Chem.* **2003**, *13*, 877–882.

(17) Koelsch, M.; Cassaignon, S.; Ta Thanh Minh, C.; Guillemoles, J.-F.; Jolivet, J.-P. *Thin Solid Films* **2004**, *451−452*, 86–92.

(18) Luo, H.; Wang, C.; Yan, Y. *Chem. Mater.* **2003**, *15*, 3841–3846.

The present paper reports on the polymer-assisted sol−gel synthesis of TiO_2 from $TiCl_4$ essentially based on the Yan method but with the aim of obtaining pure (anatase or rutile) and mixed-phase powders only by controlled modification of H_2O:Ti (r_w) and HCl:Ti (r_a) molar ratios. A rationale was suggested for the employed r_w and r_a values.

The crystalline structure, morphology, particle size, and shape of the sol−gel TiO_2 were investigated and related to the catalytic activity in the photomineralization of phenol by homogeneous (H_2O_2) and heterogeneous (O_2) oxidative agents in order to provide evidence for the different catalytic mechanisms active in the two experimental procedures. The conclusions were compared with those reported for hydrothermal TiO_2.[10]

Electron and hole pairs generated by UV irradiation and trapped in TiO_2 were investigated by EPR in order to relate their stability to the crystalline phase, particle shape and size, and surface properties. Suggestions for relations with the photocatalytic mechanism were also drawn. To the best of our knowledge, this is the first time that the properties of paramagnetic defects in TiO_2 have been related to the photoactivity.

2. Experimental Section

2.1. TiO_2 Synthesis. TiO_2 powders were prepared by the sol−gel process using a triblock copolymer as a templating agent. Reagents were titanium(IV) chloride ($TiCl_4$ (purity ≥ 99.9%)), triblock copolymer $EO_{20}-PO_{70}-EO_{20}$ (Pluronic P123, EO = $-CH_2CH_2O-$, PO = $-CH_2(CH_3)CHO-$), ethanol (EtOH (purity ≥ 99.9%)), HCl (37 wt % aqueous solution), phenol (purity ≥ 99%), and H_2O_2 (35 wt % aqueous solution) from Aldrich. Commercial TiO_2 Degussa P25 was purchased from Degussa Corp. All chemicals were used as received. Mill-Q water was used.

In a typical synthesis, 1.0 g of Pluronic P123 was dissolved in 10.0 g of EtOH under magnetic stirring. $TiCl_4$ (1.00×10^{-2} mol) was added dropwise under a N_2 atmosphere, and the solution was vigorously stirred for 30 min; then Mill-Q water was added to the solution ($r_w = 0{:}33$ molar ratio).

A second series of TiO_2 samples was prepared by varying the solution acidity. In this case aqueous HCl (37 wt %) was added to the $TiCl_4$ solution ($r_a = 0{:}15$ molar ratio) and the amount of water depended on the added HCl solution ($r_w = 0{:}52$ molar ratio).

Sols were maintained at 40 °C in a dry air stream (35 cm^3/min); care was taken so that all samples had the same area of exposed surface (∼24 cm^2). Transparent gels formed after 3−13 days depending on r_w and r_a. Gelation times were taken when the sol phase transformed into continuous phase, incorporating the total amount of solvent and holding the shape of the container. Afterward, gels were aged for 12 h, and subsequently, they were dried in air at 78 °C for 24 h. The resulting xerogels were calcined in flowing O_2 (70 cm^3/min) at 300 °C for 10 h and 400 °C for 5 h in order to completely remove the organics and obtain a white crystalline TiO_2 powder.

Table 1 summarizes the synthesis conditions, the values of r_w and r_a, and the phase composition of the annealed samples calculated from XRD analysis (see section 2.2: TiO_2 Characterization Methods).

A selected number of TiO_2 samples (Table 1) were prepared in the absence of copolymer in order to investigate its influence on the powder properties.

Table 1. Synthesis Conditions and Phase Composition of TiO_2 Powders after Calcination at 400 °C

sample	r_w	r_a	P123	gelation time (days)	phase (%)[a] anatase	rutile
SG1	0.0	0.0	yes	3	100	
SG2	6.0	0.0	yes	7	78	22
SG3	10.0	0.0	yes	5	66	34
SG4	15.0	0.0	yes	6	48	52
SG5	23.0	0.0	yes	6		100
SG6	33.0	0.0	yes	7		100
SG7	16.5	4.8	yes	7	71	29
SG8	33.0	9.6	yes	12	20	80
SG9	52.0	15.0	yes	13	14	86
SG10	0.0	0.0	no	5	100	
SG11	23.0	0.0	no	5	100	
SG12	16.5	4.8	no	7	100	

[a] From XRD measurements.

The reproducibility of the phase content was verified by repeating each synthesis three times. The variance in the phase composition was about ±5 wt %.

2.2. TiO_2 Characterization Methods. X-ray diffraction (XRD) patterns were collected with a Bruker D8 Advance diffractometer (Cu Kα radiation) in the range 20−40° 2θ (2θ step 0.020°, counting time of 2 s per step). The diffraction peaks were indexed as pure rutile TiO_2 (JCPDS, no. 21-1276) and pure anatase (JCPDS, no. 21-1272). Brookite was never detected. Analyses were performed on the annealed powders and selected xerogels. In the latter case the copolymer was dissolved in methanol and the solid recovered by centrifugation. The phase contents were estimated from the respective XRD peak intensities using the following equation[19]

$$f_A = \frac{1}{\left(1 + \frac{1}{K}\frac{I_R}{I_A}\right)} \quad (1)$$

where f_A is the fraction of the anatase phase in the powder; $K = 0.79$ when $f_A > 0.2$ and $K = 0.68$ when $f_A < 0.2$; I_R and I_A are the integrated intensities of the rutile 110 and anatase 101 peaks, respectively.

The average crystallite size of TiO_2 was estimated from the broadening of the XRD peaks 110 for rutile and 101 for anatase by means of the Scherrer equation ($D = K\lambda/\beta \cos\theta$, where D is the average crystallite size, $K = 0.94$ is a constant, λ is the X-ray wavelength, β is the full-line width at half-maximum corrected for the instrumental broadening, and θ is the diffraction angle).

Nitrogen physisorption measurements were carried out on a Micromeritics ASAP 2010. The specific surface area (SSA, BET method), pore volume (desorption cumulative pore volume, DCPV), and pore size distribution (BJH method) of selected samples were measured after evacuation at 473 K for 12 h.

High-resolution transmission electron microscopy (HRTEM) and electron diffraction (ED) experiments were performed using a Jeol 3010 apparatus operated at 300 kV with a high-resolution pole piece (0.17 nm point-to-point resolution) and equipped with a Gatan slow-scan 794 CCD camera. The powders were suspended in isopropyl alcohol, and a 5 μL drop of this suspension was deposited on a holey carbon film supported on a 3 mm copper grid for TEM investigation.

EPR spectra were recorded on a Bruker EMX spectrometer working at the X-band frequency, equipped with an Oxford cryostat operating in the temperature range 4−298 K. Spectra were recorded on powder samples under a helium atmosphere at 10 K after 20 min of irradiation at this temperature inside the EPR cavity. One

(19) Mazdiyasni, K. S. *Ceram. Int.* **1982**, *8*, 42.

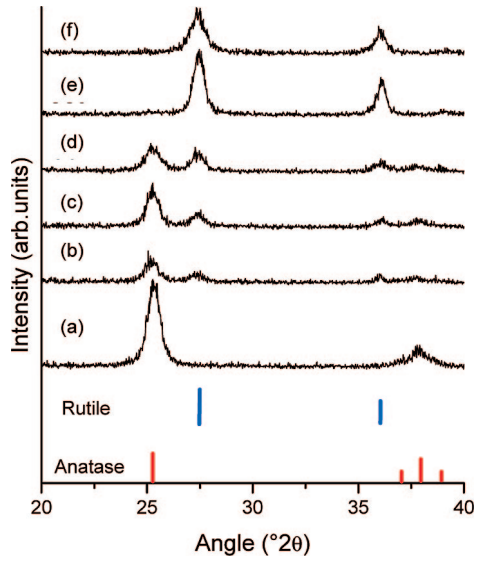

Figure 1. XRD patterns of TiO_2 samples synthesized from an ethanol solution of $TiCl_4$ with different $r_w = H_2O$:Ti molar ratios after calcination at 400 °C: (a−f) r_w = 0, 6, 10, 15, 23, and 33 (samples SG1−SG6, respectively). The vertical lines indicate the position and intensity of anatase and rutile reflections.

and 20 min after switching off the lamp, the spectra were newly recorded. The modulation frequency was 100 kHz, modulation amplitude 3−10 gauss, and microwave power 5−10 mW. For each sample the absence of a signal before irradiation was checked. Irradiation was performed by a UV 500W Hg lamp (Jelosil, Italy) with the output radiation focused on the samples in the cavity using an optical fiber (50 cm length, 1 cm diameter).

The g values were determined by standardization with α,α′-diphenyl-β-picryl hydrazyl (DPPH). The spin concentration was calculated by double integration of the resonance lines, referring the area to that of the standard Bruker weak pitch ($9.7 \times 10^{12} \pm$ 5% spins cm^{-1}). Care was taken to assume that the most sensitive part of the EPR cavity (1 cm length) was always filled. Spectra simulation and fit were performed using the SIM 14S program.[20]

2.3. Photoinduced Degradation of Phenol. Photodegradation experiments were carried out in a 400 mL pyrex discontinuous batch reactor with an external cooling jacket, enveloped by aluminum foil, and equipped with a UV 125 W Hg high-pressure lamp that was placed in a coaxial quartz cylinder. No optical filter was adopted. Titanium dioxide (100 ± 5 mg) was suspended by sonication in 400 mL of water containing 121 ± 2 ppm of PhOH (93 ± 2 ppm as C). The temperature was kept at 25 ± 2 °C, and the suspension was recirculated by a peristaltic pump (14 mL s^{-1}). The pH and oxygen content were monitored by online sensors.

Photodegradation was performed in the presence of H_2O_2 or O_2 as oxidative agent. In the former case, a stoichiometric amount of 35 wt % H_2O_2 aqueous solution was added ($PhOH/H_2O_2$ = 14 mol/mol) and the suspension was circulated in the dark for 30 min before turning on the UV source. In the latter case, the suspension was circulated in the dark and saturated in an online chamber by continuously bubbling oxygen (100 mL min^{-1}); the excess gas was eliminated through a nonreturn check valve. The UV source was turned on when the oxygen content in the suspension was maximum and constant (in about 10 min). The reaction was performed keeping the oxygen feed constant. In both cases control experiments were carried out in the absence of TiO_2 (blank) and with Degussa P25.

(20) Lozos, G. P.; Hofman, B. M.; Franz, C. G. *Quantum Chemistry Program Exchange* **1973**, 65.

In order to monitor the photoinduced degradation of phenol, aliquots (6 mL) of the reaction solution were drawn out at regular intervals. Then TiO_2 powder was separated by centrifugation, and the clear solution was analyzed for the total organic carbon (TOC) using a Shimadzu TOC-V CSH analyzer.

3. Results and Discussion

3.1. Synthesis and Phase Composition. The synthetic approach proceeds from that proposed by Yan et al.[18] Addition of the strong Lewis acid $TiCl_4$ to an alcoholic solution containing the block copolymer produces Ti(IV) chloro-alkoxides and HCl, according to reaction 2[21]

$$TiCl_4 + xROH \rightleftarrows TiCl_{4-x}(OR)_x + xHCl \quad x \approx 2 \qquad (2)$$

Water was then added to the resulting acidic solution and promoted hydrolysis and condensation of $TiCl_{4-x}(OR)_x$ and gel formation following the reactions

$$TiCl_{4-x}(OR)_x + zH_2O \rightleftarrows TiCl_{4-z}(OH)_z + yHCl + xROH \quad z = x + y \qquad (3)$$

$$2{\equiv}Ti{-}OH \rightleftarrows {\equiv}Ti{-}O{-}Ti{\equiv} + H_2O \qquad (4)$$

$${\equiv}Ti{-}OH + {\equiv}Ti{-}Cl \rightleftarrows {\equiv}Ti{-}O{-}Ti{\equiv} + HCl \qquad (5)$$

It was reported that different amounts of water and HCl modify the relative abundance of the crystalline phases in TiO_2.[18] However, neither details to achieve strict control of the phase composition were given nor the rationale for the synthesis conditions was suggested. Thus, in the present paper r_w and r_a were systematically varied and the copolymer effect was investigated in order to set the reaction conditions suitable to achieve fine tuning of theTiO_2 phase composition.

Effect of r_w. The synthesis was performed in ethanol without further HCl addition with r_w = 0, 6, 10, 15, 23, and 33 (samples SG1−SG6 in Table 1). For r_w = 0 (SG1), gelation occurs within 3 ± 0.5 days, while the time increased to 6–7 ± 0.5 days when $r_w \neq 0$ (SG2−SG6). The XRD patterns in Figure 1 show the crystalline phase composition of some synthesized TiO_2 powders after calcination al 400 °C. By increasing the r_w value, the phase composition changes from pure anatase to pure rutile, passing through mixed-phase materials (Table 1 and Figure 2).

In particular, when r_w = 0, pure anatase is obtained (SG1); by increasing r_w ($6 < r_w < 15$), mixed-phase samples with increasing rutile content are obtained (SG2−SG4); finally, when $r_w \geq 23$, only the rutile phase results (SG5 and SG6). In no case was brookite obtained. As the amount of water was increased, the solution volume changes and the titanium concentration in the sol phase decreases. The plot in Figure 3 shows the inverse dependence of the rutile content on the titanium concentration, reported as mol·kg^{-1}.

XRD analysis was also performed on gels dried at 78 °C. These patterns show that in the case of rutile-rich samples, rutile nanocrystals (XRD size ≈ 4−5 nm) are dispersed in the xerogel. On the contrary, in the case of pure anatase samples, only the amorphous solid is present, even if nucleation of undetectable anatase seeds cannot be excluded.

(21) Bradley, D. C.; Mehrotra, R. C.; Rothwell, I. P.; Singh, A. *Alkoxo and Aryloxo Derivatives of Metals*; Academic Press: London, San Diego, 2001; Chapter 2.

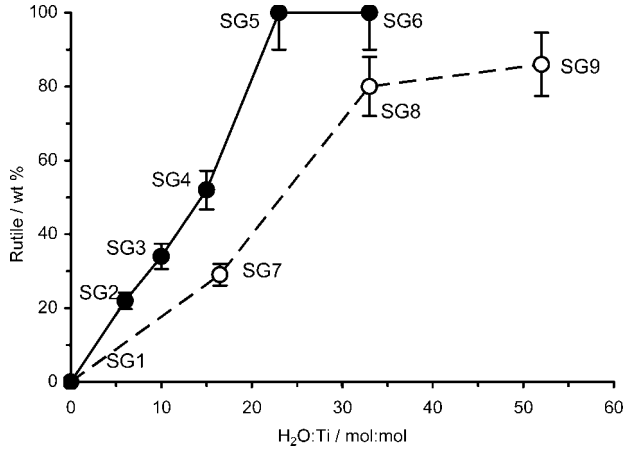

Figure 2. Plots of rutile content (wt %) in TiO_2 samples after calcination at 400 °C, synthesized from an ethanol solution of $TiCl_4$, vs H_2O:Ti molar ratio: (●) samples synthesized with different r_w and (○) samples synthesized with different r_a. Continuous and dashed lines are for guiding the eye only.

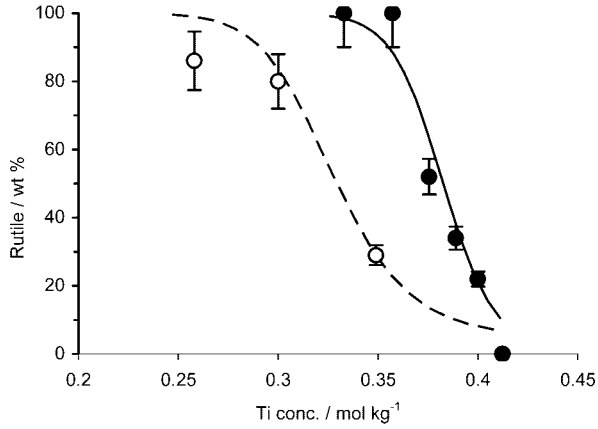

Figure 3. Plots of rutile content (wt %) in TiO_2 samples after calcination at 400 °C, synthesized from an ethanol solution of $TiCl_4$ vs titanium concentration: (●) samples synthesized with different r_w and (○) samples synthesized with different r_a. Fitting curves are calculated according eq 6.

Effect of r_a. Titania powders were also synthesized by adding different amounts of aqueous HCl to an ethanol solution of $TiCl_4$ (Table 1): $r_a = 0$, 4.8, 9.6, and 15 (samples SG1, SG7, SG8, and SG9). The total HCl content will be the amount added as well as that formed during alcoholysis and hydrolysis of $TiCl_4$ (reactions 2, 3, 5). After addition of HCl 37%, the r_w ratio is 0 (SG1), 16.5 (SG7), 33 (SG8), and 52 (SG9) (Table 1). Gelation times increased by addition of aqueous HCl, mainly at high r_a (Table 1).

XRD data showed that the percentage of rutile increases with increasing HCl content (Table 1). However, considering the overall water content, in fact addition of HCl lowers the amount of rutile for the same r_w (Figure 2) and Ti concentration (Figure 3) values.

Effect of the Block Copolymer. Syntheses performed in the absence of the block copolymer gave only pure anatase, independently of r_w and r_a values (samples SG10−SG12 in Table 1).

The dependence of TiO_2 phase composition on the synthesis parameters may be reproduced by the following empirical equation, relating the anatase:rutile ratio with the concentration of both titanium and acid

$$\frac{A}{R} = K[\mathrm{Ti}]^{\alpha}[\mathrm{H}]^{\beta} \qquad (6)$$

where A and R are the weight fraction of anatase and rutile, respectively, and [Ti] and [H] are the overall titanium and acid concentration (expressed as mol kg^{-1}), which are also representative of the water quantity. Complete hydrolysis of $TiCl_4$ was assumed. Optimal values of K, α, and β (4.69×10^9, 25.2, and 4.6, respectively) were obtained by fitting the experimental rutile weight fraction data (see Figure 3).

The above results suggest that rutile precipitation and amorphous gel formation are competitive processes, which depend on the titanium concentration in the starting acidic sol. In fact, condensation reactions 4 and 5 occur between octahedral $TiCl_{4-z}(OH)_z$ units ($1 \le z \le 4$; coordinated water not indicated). Octahedral units may share the edges in a line (basic structural unit of rutile) or in a right-angle array (basic structural unit of anatase).[22] The former configuration, which has a larger $Ti^{4+}-Ti^{4+}$ distance, is thermodynamically more stable since it minimizes the electrostatic repulsions; for this reason it is favored at lower reaction rates. The latter configuration is statistically favored since the octahedral units may share several edges to form a right-angle array and is thus preferred at higher reaction rates. Therefore, since the higher the titanium concentration (lower amount of added water) the higher the probability of random organization of octahedral units, at higher titanium concentrations formation of an amorphous gel prevails. On the other hand, at lower titanium concentrations the rate of condensation processes 4 and 5 decreases as shown by the increase of gelation times (Table 1), so that rutile nucleation is favored. These competitive mechanisms only occur in the presence of the copolymer, which allows one to obtain rutile, besides anatase, by varying r_w and r_a. The effect may be due to interaction of PEO/PPO with Ti^{4+} centers. In fact, it was demonstrated that the metal centers can be chelated by the ether functions of the PEO or PPO chains; if large quantities of water are present, hydrophilic titanium oxo oligomer units interact with the polymer by H bonds.[23,24] As a consequence, the hydrolysis and condensation processes slow down, favoring formation of the rutile phase.

As for the role of acidity, the following consideration can be made. Using $TiCl_4$ as precursor, hydrolysis and condensation reactions occur in acidic conditions due to HCl released in reactions 2, 3, and 5. When more HCl is added, the electrostatic repulsion between TiO_2 subunits increases due to chemisorbed charged species, hindering the units aggregation.[25] This could lead to partial inhibition of rutile nucleation and produce a higher amount of anatase in samples prepared with the same r_w and titanium concentration but $r_a \neq 0$.

In conclusion, the synthesis parameters determine the nature of seeds in the xerogels. After calcination at 400 °C, seed-induced crystallization occurs and the phase composition of the products is a consequence of the nature of the

(22) Gopal, M.; Moberly Chan, W. J.; De Jonghe, L. C. *J. Mater. Res.* **1997**, *32*, 6001–6008.
(23) Soler-Illia, G. J. A. A.; Sanchez, C.; Lebeau, B.; Patarin, J. *Chem. Rev.* **2002**, *102*, 4093–4138.
(24) (a) Soler-Illia, G. J. A. A.; Scolan, E.; Louis, A.; Albouy, P. A.; Sanchez, C. *New J. Chem.* **2001**, *25*, 156–165. (b) Soler-Illia, G. J. A. A.; Sanchez, C. *New J. Chem.* **2000**, *24*, 493–499.

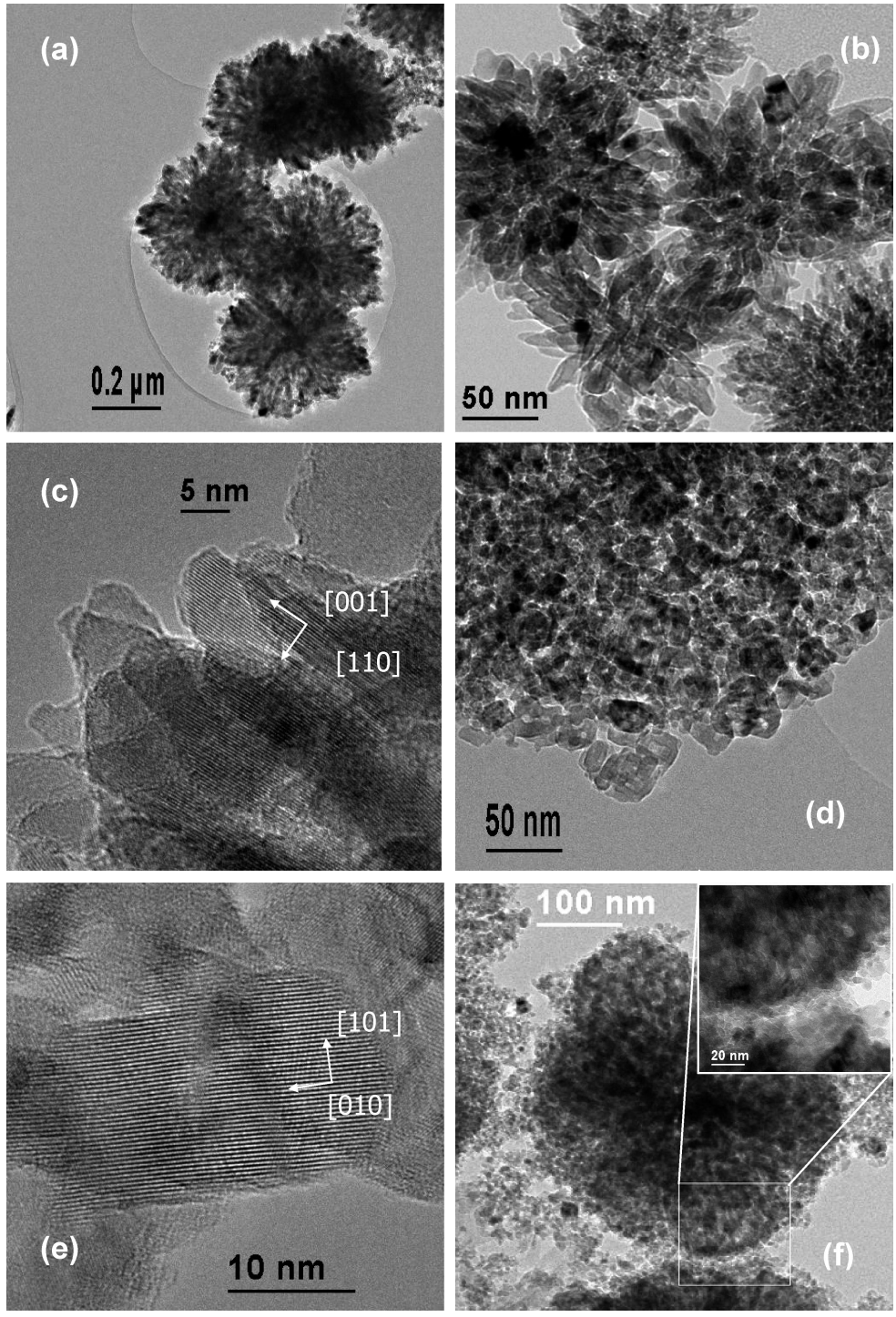

Figure 4. TEM (a, b, d, f) and HRTEM (c, e) images of (a−c) pure rutile (SG6), (d, e) pure anatase (SG1), and (f) mixed anatase 48 wt % and rutile 52 wt % sample (SG4).

xerogel.[22] If no rutile particles are present in the xerogel, thermal treatment promotes nucleation and growth of anatase. In the presence of a relevant amount of rutile seeds, rutile growth prevails over anatase and pure rutile samples are obtained. Anatase−rutile mixed-phase samples are obtained in the intermediate cases.

3.2. Morphological Characterization of TiO_2. TEM and HRTEM micrographs of some representative samples (SG1, SG6, SG4) are shown in Figure 4. No amorphous surface layers were detected. Pure rutile phase (Figure 4a, 4b, 4c) shows chestnut burr aggregates of radially growing elongated nanocrystals with average sizes of 10−20 nm in width and 100−200 nm in length. HRTEM micrographs show that rutile particles grew in the [001] direction with $\alpha \approx 8-10$.

Pure anatase phase (Figure 4d, 4e) shows aggregates of almost square-ended nanoparticles with average sizes of 5−15 nm. Particles have $\alpha \approx 1-3$ and show preferentially the {100} surface.

(25) Serrano, D. P.; Calleja, G.; Sanz, R.; Pizarro, P. *J. Mater. Chem.* **2007**, *17*, 1178–1187.
(26) Wang, C. C.; Ying, J. Y. *Chem. Mater.* **1999**, *11*, 3113.

In Figure 4f, TEM micrographs show an example of mixed-phase sample (SG4, anatase 48%−rutile 52%). The presence of the two phases is confirmed by the corresponding ED pattern (not shown). Sizes and shapes of rutile and anatase crystals reflect those observed in the corresponding pure phase samples, with the small anatase particles surrounding the chestnut burr aggregates of rutile.

The average crystalline size calculated from the broadening of XRD 101 anatase peak were about 10−14 nm, in agreement with TEM results. As the rutile crystals grow along the *c* axis, the particle size calculated from the broadening of XRD 110 peaks, 10−15 nm, corresponds to the width of the crystal.

Nitrogen physisorption analyses were performed on selected samples. All samples were mesoporous, showing type 4 Brunauer[27] isotherm. According to the t-plot[28] (not reported), no micropores were detected.

Both the pure anatase and mixed-phase (e.g., SG2, anatase: rutile 78:22 in Figure 5b) samples show a monomodal pore size distribution in the range 3−20 nm, a specific surface area (SSA) of 120−130 $m^2\ g^{-1}$, and a DCPV of 0.37−0.40 $cm^3\ g^{-1}$. Pure rutile sample shows an unusually high SSA of 113 $m^2\ g^{-1}$ and DCPV of 0.37 $cm^3\ g^{-1}$. In addition, the narrow and extended hysteresis loop (Figure 5a) can be classified as H3, according to IUPAC.[29] Isotherm H3 corresponds to a disordered pore size distribution as a consequence of the particular chestnut burr morphology of the aggregates. The high rutile SSA, in spite of its larger crystallite dimensions, can be explained by the less compact aggregation of chestnut burr particles with respect to the small cubic crystals of anatase (see Figure 4).

Although the water/polymer/solvent ratios used in the synthesis should, in principle, promote the micelle template mechanism,[23] in the present case no ordered mesostructures of TiO_2 were obtained. This result may be explained referring to the high acidity of the reaction solution. In fact, the large amount of HCl generated from hydrolysis of $TiCl_4$ prevents cross-linkage of the titania framework leading to a wormlike structure,[30] probably due to the chemisorbed charged species that induce electrostatic repulsion between TiO_2 subunits.

In fact, pure anatase samples prepared without copolymer (e.g., SG10 in Figure 5c) show a lower SSA, 75 $m^2\ g^{-1}$, and DCPV, 0.16 $cm^3\ g^{-1}$, a bimodal pore size distribution with a maximum in the range 3−7 nm, and a shoulder between 7 and 20 nm. Thus, the copolymer, besides allowing compositional control, really promotes high SSA and porosity whatever the phase composition. Moreover, the equivalent BET particle size, calculated according to the equation

$$d_{BET} = \frac{6}{\rho(SSA)} \tag{7}$$

is about 20 nm for SG10, significantly higher than the crystallite size calculated from XRD, 14 nm (see Table 1), suggesting that a fraction of the surface is not available to nitrogen physisorption and that the particles could be more aggregated with respect to anatase samples prepared with the copolymer.

3.3. Photocatalytic Activity. The photocatalytic activity of the sol−gel-obtained TiO_2 samples was measured in the phenol mineralization with H_2O_2 under UV irradiation (see Experimental Section). A selected number of samples were also tested in the photomineralization with O_2.

The catalyst performance was evaluated by fitting the experimental data (TOC vs time) with the function

$$TOC(t) = C_0 - A\int_0^x \exp\left(-\frac{(t-t_0)^2}{s}\right)dt \tag{8}$$

where C_0, A, t_0, and s are the fitting parameters (C_0 is the total organic carbon in solution before phenol degradation

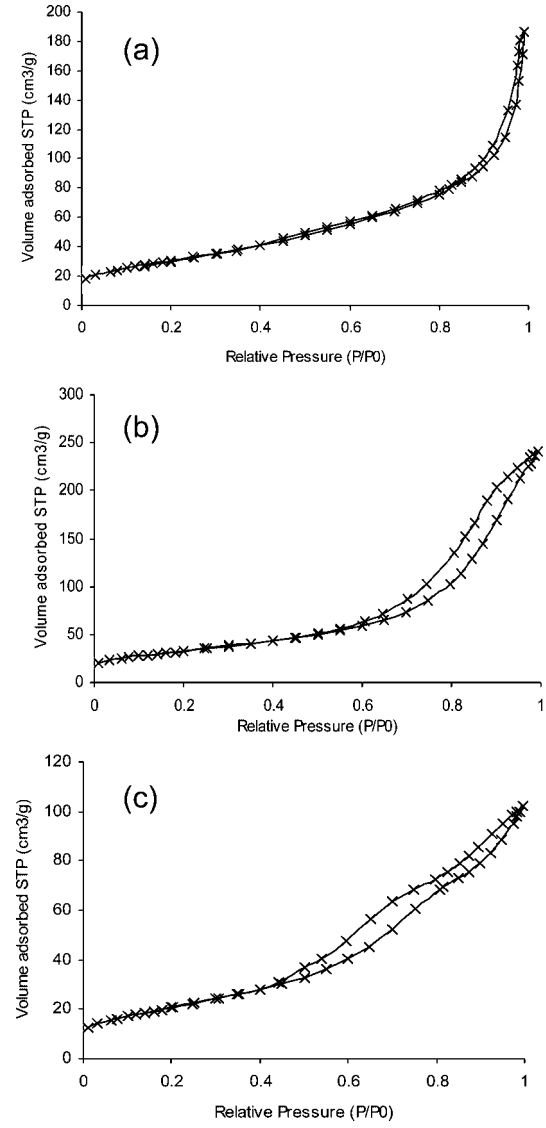

Figure 5. Nitrogen adsorption isotherms of (a) pure rutile (SG6), (b) mixed anatase 78 wt % and rutile 22 wt % sample (SG2), and (c) pure anatase prepared in the absence of copolymer P123 (SG10).

(27) Brunauer, S.; Emmet, P. H.; Teller, E. *J. Am. Chem. Soc.* **1940**, *62*, 1723.
(28) Lippens, B. C.; de Boer, J. H. *J. Catal.* **1965**, *4*, 319.
(29) Sing, K. S. W.; Everett, D. H.; Haul, R. A. W.; Moscou, L.; Pierotti, R. A.; Rouquerol, J.; Siemieniewska, T. *Pure Appl. Chem.* **1985**, *4*, 603–619.
(30) (a) Chen, L.; Yao, B.; Cao, Y.; Fan, K. *J. Phys. Chem. C* **2007**, *111*, 11849–11853. (b) Wan, Y.; Yang, H.; Zhao, D. *Acc. Chem. Res.* **2006**, *39*, 423.

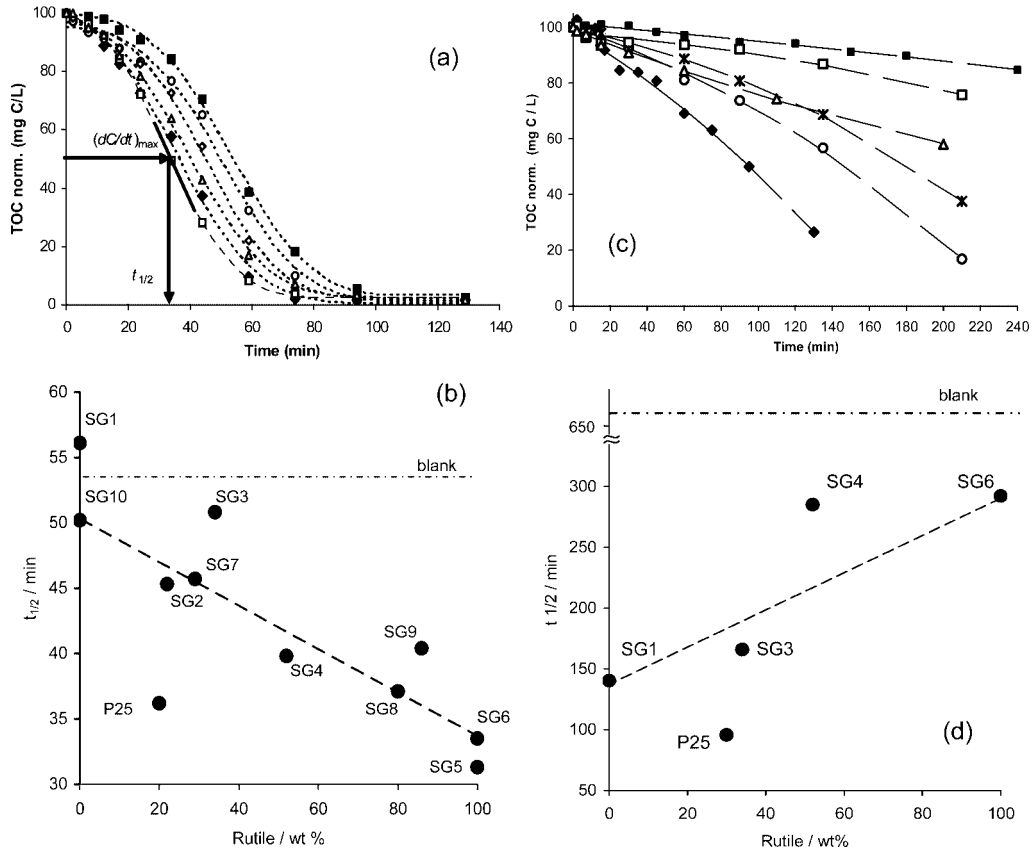

Figure 6. Mineralization curves of phenol (TOC %) in the presence of some representative catalysts ((♦) P25, (□) SG6, (△) SG4, (×) SG3, (◊) SG2, (○) SG8, (■) blank) using (a) H_2O_2 and (c) O_2 as oxidative agents. The dashed lines are the best fit to experimental data according to eq 8. The tangent straight line corresponds to the maximum mineralization rate ((d*C*/d*t*)max). The arrows indicate the half-transformation time ($t_{1/2}$). Half-transformation time, $t_{1/2}$, against rutile content in reactions using (b) H_2O_2 and (d) O_2. Dashed lines in b and d are guides for the eye.

and t_0 the time at which mineralization of the organic substrates starts). Figure 6a and 6c shows the mineralization curves with H_2O_2 and O_2, respectively, for some representative samples and the reference experiments (blank and Degussa P25).

In order to compare the mineralization kinetics of the different samples, the maximum slope point, which corresponds to the maximum degradation rate, $(dC/dt)_{max}$, and the time value, $t_{1/2}$, calculated from eq 8, were taken as representative parameters (Table 2, where starred samples underwent oxidation with O_2). The $(dC/dt)_{max}$ and $t_{1/2}$ values were normalized to the same mass (100 mg) of TiO_2.

The photoactivated process can be described by the following reactions[6]

$$TiO_2 \xrightarrow{h\nu} e^- + h^+ \quad (9)$$

$$e^- + h^+ \rightarrow \text{energy} \quad (10)$$

$$OH^- + h^+ \rightarrow OH^\bullet \quad (11)$$

$$H_2O_2 + e^- \rightarrow OH^\bullet + OH^- \quad (12)$$

$$O_{2,gas} + 2H_2O_{ads} \rightarrow 2H_2O_{2,ads} \quad (13)$$

$$O_{2,gas} + e^- \rightarrow O_2^- \quad (14)$$

$$OH^\bullet + S \rightarrow CO_2 + H_2O \quad (15)$$

Photons with energy equal to or higher than the band gap (E_g) promote formation of electron−hole (e^-, h^+) pairs (eq 9). Charge carriers can be trapped as $Ti^{3+}$and O^- defect sites in the TiO_2 lattice; alternatively, they can recombine (eq 10) or generate $OH^\bullet$ radicals (eqs 11 and 12). Hydroxyl radicals react with the organic substrates (S) until complete mineralization (eq 15) due to their high oxidizing potential (2.80 eV). Hydrogen peroxide is directly supplied or produced by gaseous oxygen (eq 13).

In our experimental conditions, when H_2O_2 is used as the oxidizing agent, $t_{1/2}$ decreases by increasing the rutile content (Figure 6b) and $(dC/dt)_{max}$ slightly increases (data not shown in figure), indicating an enhancement in the photocatalytic activity. The best performances occurred for samples SG5 and SG6, consisting of pure rutile made up of chestnut burr nanocrystals. Their photocatalytic activities are comparable or slightly higher than Degussa P25. On the other hand, samples containing pure anatase, such as SG1, showed the lowest photocatalytic activity with respect to the mixed-phase or pure rutile powders.

These results suggest that for the sol−gel-obtained TiO_2 samples, the electron−hole recombination process has an important role in the photodegradation rate of phenol performed by homogeneous oxidant. The elongated crystals in the chestnut burr aggregates of the most reactive rutile are larger and have a higher aspect ratio than anatase nanoparticles (see HRTEM and TEM analysis). This shape and size do not favor recombination of the electron−hole pairs and promote the catalytic activity.[31–36]

Table 2. Photocatalytic Properties of Selected Titania Samples in Reactions Performed with H_2O_2 and O_2 (asterisked samples)

sample	rutile (wt %)	$(dC/dt)_{max}$ (ppm/min)	$t_{1/2}$ (min)
blank		1.9	54
blank*		0.070	657
P25	20	2.0	36
P25*	20	0.70	96
SG1	0	1.7	56
SG1*	0	0.43	140
SG2	22	2.0	45
SG3	34	1.8	51
SG3*	34	0.32	166
SG4	52	1.9	40
SG4*	52	0.27	285
SG5	100	2.4	31
SG6	100	2.3	34
SG6*	100	0.12	292
SG7	29	2.0	46
SG8	80	1.8	37
SG9	86	2.2	40
SG10	0	2.1	50

Comparable photocatalytic experiments performed on hydrothermal TiO_2 samples revealed a similar trend:[10] $t_{1/2}$ decreases and $(dC/dt)_{max}$ increases by increasing the rutile content and/or particle size. The highest photocatalytic activity was observed for faceted, well-crystallized, and relatively large prismatic rutile crystals having a higher aspect ratio α.

If O_2 is the oxidizing agent (Table 2, asterisked labels) the photocatalytic activity is generally lower than in the case of H_2O_2 as $OH^\bullet$ radicals are not produced by H_2O_2 decomposition. At variance with H_2O_2, the reactivity increases with the amount of anatase. In line with the high ability of anatase to chemisorb O_2 as O_2^-, demonstrated by the photoconductance measurements of Sclafani,[6] it may be suggested that oxygen interacts with the surface of anatase particles and traps the electrons according to eq 14.[37] This extends the independent lifetime of electrons and holes, decreasing the electron−hole recombination rate[8a,37] also in small particles. In addition, O_2^- centers may further generate $OH^\bullet$ radicals according to the reactions[6,37]

$$O_2^- + H_2O \rightarrow HO_2^\bullet + OH^- \quad (16)$$

$$2HO_2^\bullet \rightarrow H_2O_2 + O_2 \quad (17)$$

$$HO_2^\bullet + H_2O + e^- \rightarrow H_2O_2 + OH^- \quad (18)$$

$$H_2O_2 + e^- \rightarrow OH^\bullet + OH^- \quad (19)$$

In conclusion, in the case of oxidation with H_2O_2 in homogeneous phase the photocatalytic activity is mainly controlled by the electron−hole recombination rate (reaction 10) and is related to the crystal size and shape of particles. Instead, when O_2 is the heterogeneous oxidant, the electron−hole recombination rate still controls the activity while depending on the surface chemisorption of the electron scavenger O_2^-.

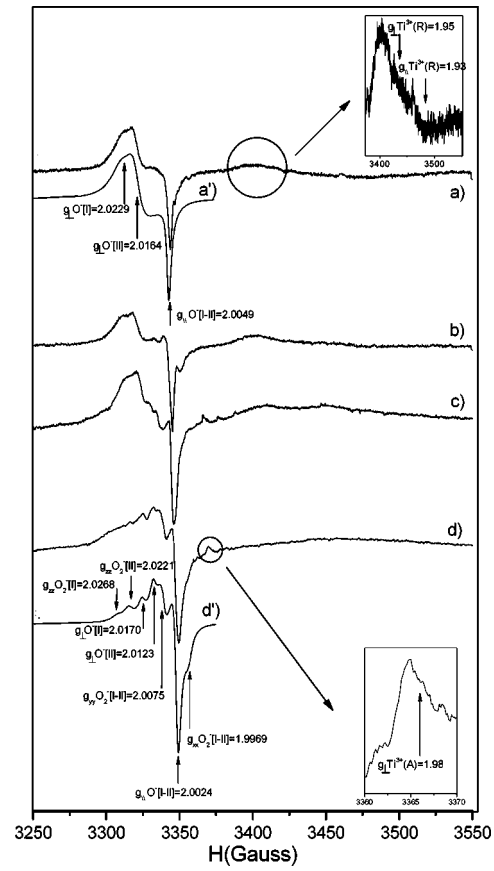

Figure 7. EPR spectra of sol−gel TiO_2 samples recorded at 10 K after 20 min of UV irradiation: (a) pure rutile (SG5), (b) anatase 48 wt % and rutile 52 wt % (SG4), (c) anatase 71 wt % and rutile 29 wt % (SG7), and (d) pure anatase (SG1). a′ and d′ simulate a and d, respectively.

It is interesting to point out that the small differences in surface area and porosity between TiO_2 crystalline phases (see morphological characterization) are not able to explain the trends of the photocatalytic properties in both oxidative conditions. The particle dimensions seem to play the major role.

3.4. EPR Characterization. EPR spectra of sol−gel-obtained TiO_2 were recorded under a He atmosphere, after UV irradiation at 10 K. The spectra were recorded 1 min after switching off UV irradiation; no significant differences resulted with the spectra recorded just before and 20 min after switching off UV irradiation, except the small decrease of the signal intensity with time.

Spectra of selected TiO_2 samples are shown in Figure 7: pure anatase (SG 1) and rutile (SG 5) samples and two mixed phases (SG 4 and SG 7) are shown.

The spectrum of rutile (Figure 7, spectrum a) shows two sets of features. The broad and poorly resolved higher field axial signals at $g_\perp = 1.95$ and $g_\parallel = 1.93$ are attributable to electrons trapped at the Ti^{3+} sites of the rutile lattice ($Ti^{3+}_{[R]}$).[7,8,9f] The lower field resonances, resolved into two different species by simulation, are attributable to holes trapped at two different O^- sites:[7–9] $O^-_{[R\text{-}I]}$ with $g_\perp = 2.0229$ and $g_\parallel = 2.0049$ and $O^-_{[R\text{-}II]}$ with $g_\perp = 2.0164$ and $g_\parallel = 2.0049$ (Figure 7, spectrum a′).

(31) Ohno, T.; Sarukawa, K.; Matsumura, M. *New J. Chem.* **2002**, *26*, 1167.
(32) Riegel, G.; Bolton, J. R. *J. Phys. Chem.* **1995**, *99*, 4215.
(33) Emilio, C. A.; Litter, M. I.; Kunst, M.; Bouchard, M.; Colbeau-Justin, C. *Langmuir* **2006**, *22*, 3606.
(34) Kominami, H.; Kato, J.-I.; Muratami, S.-Y.; Ishii, Y. A.; Kohno, M.; Yabutani, K.-I.; Yamamoto, T.; Kera, Y.; Inoue, M.; Inui, T.; Ohtani, B. *Catal. Today* **2003**, *84*, 181.
(35) Du, Y.; Rabani, J. *J. Phys. Chem. B* **2003**, *107*, 11970.
(36) Baiju, K. V.; Shukla, S.; Sandhya, K. S.; James, J.; Warrier, K. G. K. *J. Phys. Chem. C* **2007**, *111*, 7612–7622.
(37) Illisz, I.; Dombi, A. *Appl. Catal., A* **1999**, *180*, 35.

Table 3. *g* Values of Paramagnetic Species Detected in Sol−Gel TiO_2

rutile	
$O^-_{[R\text{-}I]}$	$g_\perp = 2.0229$; $g_\parallel = 2.0049$
$O^-_{[R\text{-}II]}$	$g_\perp = 2.0164$; $g_\parallel = 2.0049$
$Ti^{3+}_{[R]}$	$g_\perp = 1.95$; $g_\parallel = 1.93$
anatase	
$O^-_{[A\text{-}I]}$	$g_\perp = 2.0170$; $g_\parallel = 2.0024$
$O^-_{[A\text{-}II]}$	$g_\perp = 2.0123$; $g_\parallel = 2.0024$
$O_2^-{}_{[A\text{-}I]}$	$g_{zz} = 2.0268$; $g_{yy} = 2.0075$; $g_{xx} = 1.9969$
$O_2^-{}_{[A\text{-}II]}$	$g_{zz} = 2.0221$; $g_{yy} = 2.0075$; $g_{xx} = 1.9969$
$Ti^{3+}_{[A]}$	$g_\perp$=1.99; $g_\parallel$ nd

The first-order approximate expressions for the *g*-tensor components of the O^- anion in axial symmetry field are[38]

$$g_\parallel = g_{zz} = g_e \tag{20}$$

$$g_\perp = g_{xx} = g_{yy} = g_e + 2\frac{\lambda}{\Delta E} \tag{21}$$

where λ is the oxygen spin−orbit coupling constant (0.014 eV[37]) and ΔE is the energy separation between the p_z orbital containing the unpaired electron and the degenerate p_x and p_y orbitals.

Larger splitting of p orbitals and, consequently, lower $g_\perp$values are expected for O^- centers close to more positively charged ions.[38] $g_\perp$ components for $O^-_{[R\text{-}I]}$ and $O^-_{[R\text{-}II]}$ can be fitted to these expressions yielding, respectively, ΔE = 1.359 and 1.985 eV. The former value is similar to those reported for defect centers like $Ti^{4+}-O-M^{3+}$;[39] the latter may be associated with $Ti^{4+}-O^-Ti^{4+}$ centers.[40]

Also, EPR spectra of anatase (Figure 7, spectrum d) show two sets of features. The very weak signal at $g = 1.99$ can be associated with the $g_\perp$ component of Ti^{3+} sites in the anatase lattice ($Ti^{3+}_{[A]}$),[7,8,9f] $g_\parallel$ being undetectable due to its very low intensity. The lower field overlapped resonances were resolved by simulation into four distinct species (Figure 7, spectrum d′). Two of them were identified as holes trapped at two O^- sites, different from those in rutile:[7−9] $O^-_{[A\text{-}I]}$, $g_\perp$ = 2.0170 and $g_\parallel$ = 2.0024; $O^-_{[A\text{-}II]}$, $g_\perp$ = 2.0123 and $g_\parallel$ = 2.0024. The $g_\perp$ components for $O^-_{[A\text{-}I]}$ and $O^-_{[A\text{-}II]}$ fitted to expression 21 yield, respectively, ΔE = 1.904 and 2.800 eV, suggesting that in anatase both O^- sites are close to more positively charged Ti^{4+} ions. The two other lines are due to oxygen-centered radicals, whose *g* values are typical of superoxide anions, O_2^-, chemisorbed on Ti^{4+} centers:[7−9] $O_2^-{}_{[A\text{-}I]}$, g_{zz} = 2.0268, g_{yy} =2.0075, g_{xx} = 1.9969; $O_2^-{}_{[A\text{-}II]}$, g_{zz} = 2.0221, g_{yy} = 2.0075, g_{xx} = 1.9969. The *g*-tensor values and assignment of all the paramagnetic species are reported in Table 3.

EPR spectra of mixed-phase TiO_2 (SG 3 and SG 9) are very similar to those of pure rutile samples whatever the amount of anatase in the observed range of compositions (Figure 7, spectra b and c), showing the $O^-_{[R\text{-}I]}$ and $O^-_{[R\text{-}II]}$ centers and the broad $Ti^{3+}_{[R]}$signal.

The amount of O^- centers is in the range $7 \times 10^{16}-1 \times 10^{17}$ spin·g^{-1}, and it is higher in pure rutile and rutile-rich samples than in pure anatase. $Ti^{3+}_{[R]}$ centers increase with rutile content ($1 \times 10^{16}-3 \times 10^{16}$ spin·g^{-1}), while $Ti^{3+}_{[A]}$ centers are substantially absent. The lower amount of Ti^{3+} with respect to O^- centers can be explained, in agreement with Diwald et al.,[8a,c] by considering that the majority of photoexcited electrons enter the conduction band instead of being trapped on Ti^{3+} centers. Such an effect is more evident for anatase than for rutile, in accordance with the higher positive charge of the Ti^{n+} centers surrounding O^- in anatase. The broadness of $Ti^{3+}_{[R]}$ resonances indicates that Ti^{3+} centers are located in a disordered environment, probably near the surface, and suggests that their energy levels are too shallow to be highly efficient electron traps.

In the mixed-phase samples, h^+ and e^- were preferentially trapped on O^- and Ti^{3+} centers of the rutile phase, even when anatase is the main component. This indicates that electron transfer occurs from the higher energy conduction band states of anatase to those of rutile at lower energy and, simultaneously, hole transfer occurs from the lower energy valence band states of anatase to those of rutile at higher energy. This charge transfer is favored by the close contact between small anatase particles and larger rutile rods, as from the TEM micrographs (Figure 4f), and stabilizes the h^+-e^- separation in the presence of rutile. Gray and co-workers[7] found that the photogenerated electrons migrate from rutile to anatase, but the opposite charge transfer was associated with atypically small rutile crystallites interwoven with anatase; when particle sizes increased, the rutile trapping sites increased.

Thus, EPR investigation suggests that rutile and mixed-phase solids, UV irradiated in the absence of oxygen, contain an amount of electron and hole traps higher than anatase, possibly in agreement with the photocatalytic activity in the homogeneous procedure (H_2O_2) where the photoactivity was connected to the amount of separated charges.

In anatase and mixed-phase samples, a certain amount of superoxide O_2^- (∼1/7 of the number of O^- centers) was observed even if UV irradiation was performed under helium atmosphere. In the absence of oxygen, formation of O_2^- on sol−gel samples may occur according to the scheme proposed by Graetzel,[40] and it is favored by the presence of hydroxyl groups in sol−gel samples

$$h^+ + OH^- \rightarrow OH^\bullet \tag{22}$$

$$2OH^\bullet \rightarrow H_2O_2 \tag{23}$$

$$H_2O_2 + h^+ \rightarrow O_2^- + 2H^+ \tag{24}$$

$$O_2^- + h^+ \rightarrow O_2 \tag{25}$$

The presence of O_2^- confirms the anatase attitude to chemisorb oxygen in a reduced form.

4. Summary and Concluding Remarks

On the basis of the sol−gel method, a synthetic approach was suggested which allowed preparation of TiO_2 with controlled phase composition. Different rutile:anatase ratios were obtained by adding water and HCl in various amounts to an alcoholic solution of $TiCl_4$ and template block copolymer. It was found that an increase of the H_2O:Ti molar

(38) Che, M.; Tench, A. J. *Adv. Catal.* **1982**, *31*, 77.

(39) Zwingel, D. *Solid State Commun.* **1976**, *20*, 397–400.

(40) Howe, R. F.; Grätzel, M. *J. Phys. Chem.* **1987**, *91*, 3906–3909.

ratio (r_w) changes the oxide composition from pure anatase to pure rutile through a number of intermediate mixtures, as well as further addition of HCl, besides that released in hydrolysis/condensation reactions, decreases the rutile amount for the same r_w. Syntheses performed in the absence of template polymer always gave pure anatase.

It was suggested that the octahedral units $TiCl_{4-z}(OH)_z$, base for the condensation in sol phase, share the edges in a line (basic structural unit of rutile) as long as the reaction rate is low (low Ti concentration), while at higher reaction rate (high Ti concentration) the octahedral units share several edges and form the right-angle array of anatase. The template polymer coordinates the metal precursor and slows the reaction favoring the rutile phase.

Pure rutile phase forms aggregates of radially growing elongated nanocrystal, 10−20 nm in width and 100−200 in length; pure anatase shows almost square-ended nanoparticles with a 5−15 nm average size. In mixed phases several small anatase particles surround the rutile aggregates.

The photocatalytic activity of rutile, anatase, and mixed-phase sol−gel samples, investigated in the phenol photomineralization, showed that when the oxidation is performed by H_2O_2 pure rutile is the most active catalyst. Under the hypothesis that electron−hole recombination is the rate-determining step among the reactions of the photoactivated process, the rutile activity can be associated to its large crystalline rod shape with high aspect ratios, which do not favor recombination of UV-generated charge carriers. Anatase is more active than rutile when the oxidation is performed by O_2 because in this case the relevant chemisorption of oxygen as O_2^- stabilizes the $e^- - h^+$ separation more than the anatase crystalline shape. Anatase has in fact a higher tendency than rutile to chemisorb O_2 and forms smaller crystalline particles. Thus, it was demonstrated that strong connections exist between the crystalline phase and the particle shape/size on one hand and the photocatalytic activity on the other in TiO_2 polymorphous forms. The same relationships were observed by us in the case of hydrothermally obtained TiO_2 samples.

EPR investigations of the paramagnetic charge carriers, obtained by UV irradiation at 10 K under an inert atmosphere, showed the resonance lines of holes trapped at O^- lattice sites and electrons trapped at Ti^{3+} sites. A parallel was observed between the amount of charge carriers of rutile and the highest photocatalytic activity in the presence of H_2O_2, although the value of the comparison is limited as the spectra were not obtained in reaction conditions. The amount of paramagnetic centers was strictly related to stable separation of h^+ and e^- pairs. Besides, Ti^{4+}-chemisorbed O_2^- centers, detected in anatase, confirmed their ability to fix molecular oxygen during the photocatalytic process. All the conclusions point to the fact that to obtain photocatalytic materials with the highest efficiency, the key factor is to produce samples with a specific crystalline phase and controlled particle size and shape.

Acknowledgment. The authors thank the Cariplo Foundation for financial support.

CM800465N